Supporting Information for

Chemical Structure and Distributions in Nickel-Nitrogen-Carbon Catalysts for CO_2 Electroreduction Identified by Scanning Transmission X-ray Microscopy

Chunyang Zhang,[1,2] Ladan Shahcheraghi,[1] Fatma Ismail, [1] Haytham Eraky,[2] Hao Yuan,[2,#]
Adam P. Hitchcock[2*] and Drew Higgins[1*]

1. Chemical Engineering, McMaster University, Hamilton, ON, Canada, L8S 4M1
2. Chemistry & Chemical Biology, McMaster University, Hamilton, ON, Canada, L8S 4M1

* co-corresponding author: aph@mcmaster.ca 905-525-9140
* co-corresponding author: higgid2@mcmaster.ca

present address: Electrical and Computer Engineering, U. Victoria, Victoria, BC, Canada

Table of Contents

Section S1 Comparison of advantages and limitations of STEM/EELS, STXM, XAS

Many techniques have been used to characterize M-N-C electro-catalysts with the objective of elucidating the structure and properties of catalytically active sites to provide mechanistic insight and inform advanced catalyst designs. **Table S1** summarizes the properties of four such techniques, three of which are used in this manuscript.

Table S1 Comparison of advantages and limitations of STEM/EELS, STXM, XAS

Technique	Spatial resolution	Energy resolution	Advantages	Limitations
ToF-SIMS (Time-of-flight mass spectrometry	~1 μm	none	Surface sensitive Direct observation of M-N-C cluster ions	Limited spatial resolution No electronic spectroscopy
STEM/EELS (Scanning transmission electron microscopy electron energy loss spectroscopy)	Atomic resolution	~1 eV	Very high spatial resolution Elemental and some speciation	Spatially localized measurements. Low energy resolution.
STXM (Scanning transmission X-ray microscopy)	Sub-40 nm	~0.1 eV	High energy and good spatial resolution. Chemical speciation. Quantitative analysis.	Moderate spatial resolution.
XAS (X-ray absorption spectroscopy)	None	~0.1 eV	High energy resolution. Bulk ensemble. Quantitative analysis.	No spatial resolution.

Time-of-flight secondary ion mass spectrometry (ToF-SIMS) was the first characterization technique to directly identify species consisting of coordinated Fe, N and C in oxygen reduction catalysts.[1,2] X-ray absorption spectroscopy (XAS) has also been widely used to characterize the local structure of transition metals and nitrogen atoms in M-N-C catalysts, leading to the observation of MN_x/C coordination environments.[3-6] XAS and ToF-SIMS are very useful since they provide ensemble-averaged information. However their limited spatial resolution means they do not give a complete picture in the case of structurally heterogeneous materials. M-N-C electrocatalysts are highly heterogeneous multi-component systems that include various MN_x/C species, along with metallic and metal-based ionic compounds (metal-oxide, metal-sulfide, etc.) distributed throughout hetero-atom doped carbonaceous particles.[7,8] Thus spatially resolved chemical speciation mapping is essential to identify the locations and distributions of the active species in M-N-C electrocatalysts. [7-12]

Scanning transmission electron microscopy (STEM) has been widely used to image M-N-C catalyst samples. Bright spots, observed by atomic resolution high angle, annular dark field (HAADF) imaging, have been interpreted as single metal atoms.[13,14] While this indicates the presence of single atoms with a

higher Z-number than carbon, rarely is evidence provided to verify that these higher Z-number atoms are the assumed M atoms, or that they are coordinated to nitrogen atoms within the carbonaceous matrix (in the form of MN_x/C). However, there are only a few reports where STEM coupled with atomic resolution electron energy loss spectroscopy (EELS) has provided detailed spectroscopic information on individual MN_x/C sites.[13,15-17] However, the spectral resolution of TEM-EELS is generally significantly lower than that achieved by synchrotron X-ray absorption spectroscopy, so that detailed speciation of the metal and the adjacent nitrogen and carbon atoms is not achieved. In addition, STEM-EELS characterization is usually only done at very localized regions (i.e., few nm^2),. For materials such as M-N-C that are highly heterogeneous, the limited area studied does not provide a comprehensive understanding of the identity, concentration and distribution of chemical species present. Thus, prior to this work, studies based on conventional characterization using either bulk averaged or very spatially localized measurements have (i) verified the presence of atomically dispersed MN_x/C sites and (ii) measured the average properties of M-N-C samples and correlated then with the activity/ selectivity/ performance of the overall catalyst. Here we use STXM along with XAS and TEM-EELS to provide a spatially-resolved, holistic understanding of the chemical species and structures present in M-N-C materials. STXM is a synchrotron-based technique which provides precise chemical speciation through near edge X-ray absorption fine structure (NEXAFS) spectroscopy[18] and quantitative, chemically selective imaging with sub-40 nm spatial resolution. While STEM-EELS can provide core level excitation spectra analogous to NEXAFS, in general, the STXM-based spectroscopy is much better quality and can be measured efficiently over much larger sample areas.

Section S2 Sample preparation for STXM

The Ni-N-C catalysts and reference compound powders were physically deposited from a dry state on either silicon nitride (SiN_x) windows (Norcada Inc), or 3 mm formvar coated Cu TEM grids (TED Pella Inc.) **(Fig. S1**). In each case poorly adhering particles and large agglomerates were removed by tapping the edge of the sample substrate on a hard surface. Early efforts to measure N 1s spectra from particles on SiNx windows were not successful, likely due to interference from the N 1s spectrum of the silicon nitride support. Therefore, N 1s measurements were conducted on samples deposited on formvar coated TEM grids. Details of the Ni-N-C samples and conditions of the measurements for each sample are included in supplementary information, **Table S2.**

Reference samples of 5,10,15,20-tetraphenyl- 21H,23H-porphine nickel (II) (NiTPP) was purchased from Sigma-Aldrich and used without further purification. The commercial nickel (II) phthalocyanine sample was found to contain a significant content of impurities, and therefore a pure sample of Nickel(II) 1,4,8,11,15,18,22,25-octabutoxy-29H,31H-phthalocyanine (O-NiPc) was provided by Professor Daniel Leznoff from Simon Fraser University. The structures of these materials are shown in **Scheme 1a** and **1b**. A metallic Ni reference sample was prepared by physical vapor deposition (PVD) of a 75 nm film of Ni

on a Cu TEM grid without formvar coating. Other reference samples - nickel oxide (NiO), nickel ammonium sulphate ($Ni(NH_4)_2(SO_4)_2$) and nickel carbonate ($NiCO_3$) - were purchased from CERAO, Fisher Scientific, and Johnson Matthey, respectively, and were used without further purification.

Figure S1 shows the two types of sample mounting used in this study. All materials are in the form of partially aggregated powders, except metallic Ni, which was measured as a physical vapour deposition (PVD) thin film. Samples were prepared by attaching the support with tape or epoxy to the trapezoidal STXM sample plate (not shown in **Fig. S1**), then dropping a spatula tip (<1 mg) on the support, then sharply tapping the STXM plate against a hard surface to detach weakly adhering large aggregates.

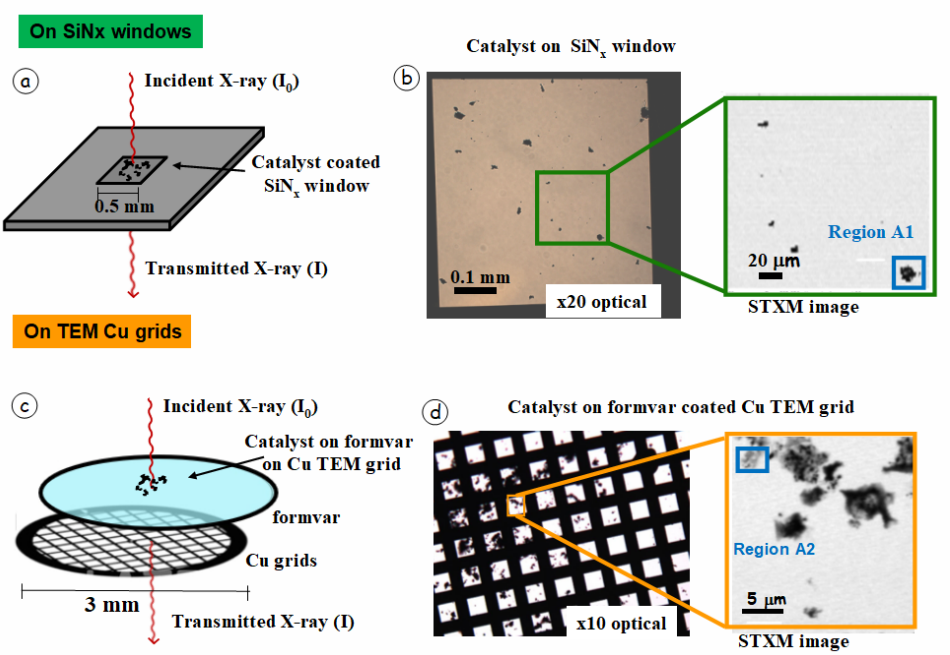

Figure S1 Sample mounting used for scanning transmission X-ray microscopy (STXM) measurements. **a)** schematic of SiNx window mounts. **b)** Transmission optical microscopy image (20x) of Ni-N-C-high particles on a SiNx window. The frame is 5 mm x 5 mm, 200 µm thick Si, with a lo-stress 0.5 mm x 0.5 mm, 75 nm thick window pane at the center (Norcada Inc) and STXM image at 395 eV of region **A1** on SiNx windows **c)** schematic of formvar coated TEM 3 mm diameter Cu grid mounts. **d)** Transmission optical microscopy image (10x) of particles Ni-N-C-high on a formvar-coated TEM Cu grids. and STXM image of one square of the TEM Cu grid sample, containing region **A2.**

After loading the sample, the STXM chamber was evacuated to ~10 Pa and then back filled with ~25 kPa of He. X-rays in the C 1s [278-330 eV], N 1s [394-432 eV], O 1s [524 – 568 eV], Ni 2p [840 – 930 eV] and S 2p [158-205 eV] energy ranges were used to study Ni-N-C catalysts and reference samples.

Section S3 Summary of samples investigated

Code	sample	substrate	edge	time	Pixel (nm)	# pixel	E - r a n g e (eV)
A1	Ni-N-C-high	SiNx	Ni 2p	2019-July	65	300*267	847.6, 852.2
A1a	Ni-N-C-high	SiNx	Ni 2p	2019-July	45	87*69	836-929
			O 1s	2019-July	45	87*69	524-568
			N 1s	2019-July	60	55*55	394-432
			C 1s	2019-July	60	51*51	278-320
A2	Ni-N-C-high	TEM grid	Ni 2p	2021-Jan	35	100*70	842-878
			O 1s	2021-Jan	35	100*70	524-568
			N 1s	2021-Jan	35	100*70	394-422
			C 1s	2021-Jan	35	100*70	278-320
			S 2p	2020-Sep	80	45*32	158-205
A3	Ni-N-C-high	TEM grid	Ni 2p	2020-Aug	80	75*75	842-900
A4	Ni-N-C-high	TEM grid	Ni 2p	2020-Aug	30	83*83	842-920
			C 1s	2020-Aug	35	72*72	278-320
A5	Ni-N-C-high	SiNx	Ni 2p	2019-July	30	103*100	840-892
			C 1s	2019-July	35	91*85	278-320
B1	Ni-N-C-low	TEM grid	Ni 2p	2020-Sep	66	60*60	842-878
			O 1s	2020-Sep	90	44*44	524-568
			N1s	2020-Sep	66	60*60	394-422
			C 1s	2020-Sep	90	44*44	278-320
B2	Ni-N-C-low	TEM grid	Ni 2p	2021-Feb	66	60*60	842-890
B3	Ni-N-C-low	TEM grid	Ni 2p	2021-Jan	35	70*70	842-878
			C 1s	2021-Jan	50	50*50	278-320
B4	Ni-N-C-low	SiNx	Ni 2p	2019-Dec	90	78*78	840-892
			C 1s	2019-Dec	90	78*78	278-320

Table S2. Details of the Ni-N-C samples and conditions of the measurements for each sample

Section S4 STXM energy calibration

We found that comparison of our spectra with results reported in the literature [19-24] was challenging due to often incomplete details regarding how the energy scales were calibrated in different studies. Especially for the Ni 2p edge, the energy of the maximum of the Ni $2p_{3/2} \rightarrow 3d$ transition in Ni metal varied by over 1 eV in the literature [24-28]. In this work, the Ni 2p spectra were calibrated by including a few torr of Ne gas in the STXM tank, such that the sharp Ne $1s \rightarrow 3p$ transition at 867.05 eV [29] was included in the same data set and thus could provide accurate calibration. Other edges were calibrated using appropriate gases whose spectra were recorded within the same injection as key catalyst or reference compounds. **Table S3** summarizes all the gas calibration features used, along with references to their calibration. **Table S4** reports the energies of the Ni $2p_{3/2} \rightarrow 3d$ peaks for the catalyst and reference compounds, in order to evaluate reproducibility.

We note that the spectromicroscopy beamline at the Canadian Light Source (CLS SM) has issues with monochromator energy scale stability which can lead to energy scale shifts between injections (typically every 8 hours), and sometimes even within a single injection. One source of this instability is slackness in the mechanical linkage driving the angle of the plane grating. A backlash protocol, consisting of slewing to 50 eV below the start energy of a spectral scan, was implemented to reduce that problem. In addition, since the optical path of the CLS SM beamline does not include an energy defining entrance slit, the energy scale can shift if there are deviations of more than 1 μm in the vertical position of the electron beam in the storage ring. Due to these factors, we occasionally found that the energy scales of the Ni 2p data sets differed by up to 1.5 eV. In the early stages of this work, energy calibration with gas standards was only performed at the start of the STXM measurements. In later runs, we calibrated before and after critical STXM measurements and used Ne gas as internal standard for Ni 2p STXM stacks (Ni metal, Ni-N-C-high), which gave more reliable results (>±0.1 eV variation). We were careful about calibrating the Ni 2p spectrum of Ni metal. Ultimately, for the critical Ni 2p analysis, we determined a value of 852.7(1) eV for Ni metal [Ni(0)] and used it as an internal standard. This is close to the energy of the Ni $2p_{3/2} \rightarrow 3d$ peak for Ni metal reported by two other groups.[26-28] We strongly encourage researchers to provide details of the energy scale calibration to enable information sharing and cross-study comparisons in the future.

Table S3 Gaseous species energy calibration

Edge	Species	Feature	Energy (eV)	ref
Ne 1s	Ne gas	Ne 1s → 3p	867.05 (8)	29
F 1s	SF_6 gas	F 1s → a_{1g}	688.3 (1)	30
C 1s	CO_2 gas	C 1s → C 3s C 1s → C 3p	292.74 (5) 294.96 (5)	31
O 1s	CO_2 gas	O 1s → O 3s	538.9 (1)	32
N 1s	N_2 gas	N 1s → 3s N 1s → 3p	406.15(2) 407.115 (5)	33

Table S4 Peak positions in catalyst and reference compound samples

samples	file	Ni (0)	Ni_3S_2	NiN_x/C	Ni(2+)
Ni metal (PVD)	A210807022	852.64 eV	-------	-------	--------
Ni metal (PVD)	A210125033	852.77 eV	---------	----------	-------
Ni-N-C-high	A210807037	852.71 eV	852.99 eV	854.19 eV	----------
Ni-N-C-high	A210120064	852.8 eV	853.1 eV	854.2 eV	--------
Ni-N-C-high	A190712097	852.75 eV	853.15 eV	854.15 eV	------
NiTPP	A210125029	----------	---------	854.08 eV	-------
Ni_3S_2	A210202019	--------	853.1 eV	----------	--------
O-NiPc	A210918047	--------	--------	854.20 eV	------
NiO	A200802045	---------	--------	-------	853.03 eV
$NiCO_3$	A200801005	---------	--------	-------	853.25 eV
$Ni(NH_4)_2(SO_4)_2$	A200801017	---------	--------	-------	853.35 eV

Section S5 STXM Data Analysis

All STXM data was analyzed using aXis2000 software. [34] The images in a stack typically drift by a few hundred nm over the 40-80 eV scan range, and therefore the stacks were aligned to ~5 nm registry using a Fourier correlation method. The transmission signal (I) of the aligned stack was converted to optical density (OD) using the Beer Lambert Law: $OD_{(x,y)} = -ln(I/I_o)$, where I is the X-ray intensity transmitted though the sample and support, and I_o is the incident X-ray intensity measured off the sample but where the X-rays transmit through all other parts of the STXM hardware (optics, windows, zone plate, detector) and the sample support (SiN_x window or formvar). After OD conversion, the C 1s, N 1s, O 1s, Ni 2p and S 2p X-ray absorption spectra (XAS) of selected areas (many pixels, which are not necessarily contiguous, but are related by spectroscopy) were extracted from the STXM stacks using methods described in greater detail below.

The fitting procedure in aXis2000, which is based on a singular value decomposition (SVD) matrix method,[35] was used to analyze the stacks. The 'stack fit' routine fits the NEXAFS spectrum at each pixel to a user-identified set of reference spectra, which can be derived from the stack itself (internal) or from spectroscopy on well defined reference compounds (external). The result of a 'stack fit' is a set of component maps (spatial distributions), one for each component, along with a map of a constant signal (no spectral variation), and the residual of the fit. [36] In cases where the set of reference spectra are known to represent all the variation in the stack signal, the 'stack fit' can be performed without the constant component (denoted 'SVD fit' in aXis2000). Internal reference spectra (which were extracted from the same STXM stack) or external reference spectra (measured in STXM from pure materials) were used at different stages in the data analysis, as explained in more detail in the results section. To quantitatively analyze the data, the external reference spectra were converted to an absolute intensity scale, optical density per nm (OD1), by scaling the relative intensity spectra until the pre-edge and far-continuum (>30 eV above the edge) match the elemental response for 1 nm thickness of the known composition and density of the reference material, which is calculated using X-ray parameters from the Centre for X-ray Optics database (https://henke.lbl.gov/optical_constants/). The gray scale of the component maps derived using OD1 reference spectra is an estimate of the thickness of that component at each pixel in the region analyzed.

Curve fits, using the same algorithm as used for stack analysis, were used to analyze spectra extracted from specific areas of a stack, identified based on morphology and / or spectral similarity. When reference spectra on OD1 intensity scales were used to curve fit a spectrum, the contribution of each spectral component is an estimate of the average thickness (in nm) of that component in the area from which the spectrum was extracted. Volume percent compositions were then estimated by combining the thickness and areal amounts. The software allows for quantization of non-contiguous areas, where the pixels of an

area are identified from their spectral properties.

Outside of the ~20-40 eV region at the onset of a given inner shell edge (the near edge X-ray absorption fine structure, NEXAFS region), the X-ray absorption of any material is only a function of its elemental composition and density.[37] Thus one can convert an X-ray absorption spectrum measured on a relative intensity scale to an absolute intensity scale, by matching the intensity of the pre-edge (e.g. -20 to -5 eV relative to the onset) and post-edge (>30 eV above the onset) NEXAFS regions to that predicted from the elemental composition and density, using tabulated elemental X-ray absorption cross-sections. [37] **Figure S2** shows the OD1 Ni 2p spectra of the 4 Ni materials used to analyze the Ni-N-C catalyst samples.

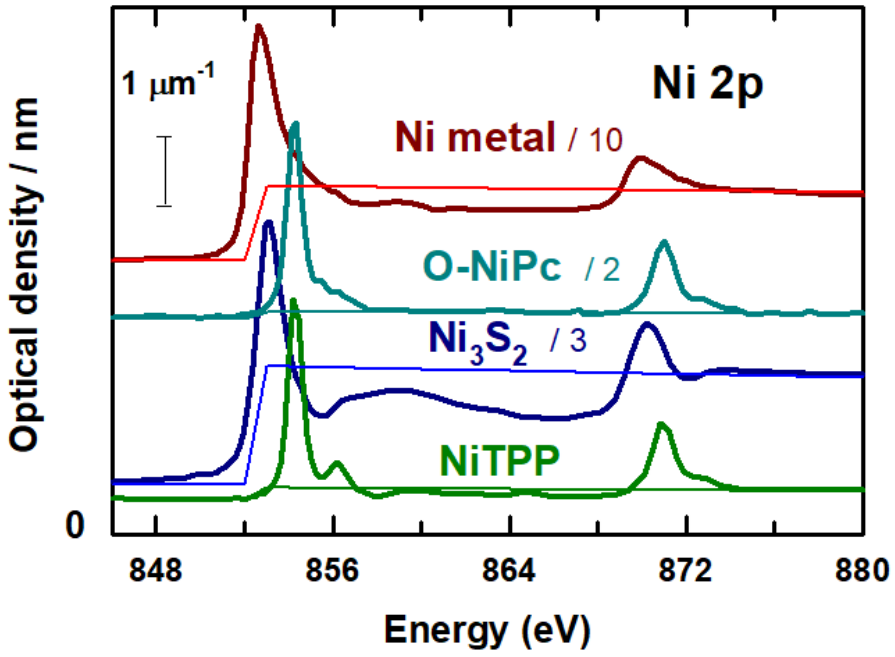

Figure S2 The quantitative Ni 2p spectra of metallic nickel (Ni(0)) (dark red), Ni_3S_2 (dark blue), O-NiPc (dark cyan) and NiTPP (dark green) on OD1 intensity scales. The step curve with corresponding color is the calculated X-ray absorption for 1 nm of elemental composition of Ni , Ni_3S_2, NiTPP ($C_{44}H_{28}N_4Ni$) and O-NiPc ($C_{64}H_{80}N_8NiO_8$), based on the response tabulated in the CXRO data base[37] and the known density of these materials (8.9 $g.cm^{-3}$ for Ni(0) [38] , 1.6 $g.cm^{-3}$ for NiTPP and O-NiPc (assume the density of NiTPP and O-NiPc same with Ni phthalocyanine) [39], and 5.8 $g.cm^{-3}$ for Ni_3S_2 [40]).

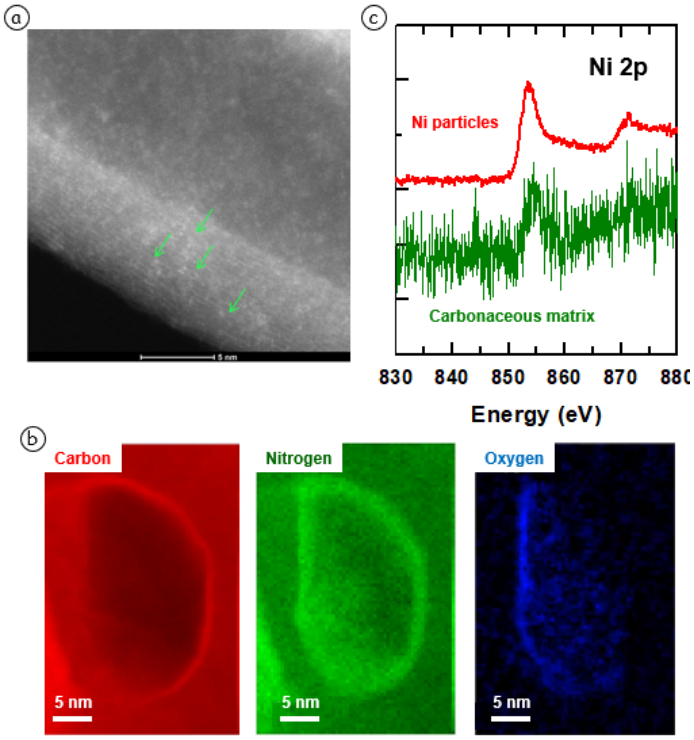

Figure S3 a) Higher resolution HAADF-STEM image. b) EELS mapping for Ni-N-C-low particles region. c) EELS spectra for Ni particles region and carbonaceous matrix region.

Section S6 STEM/EELS results for C, N, O of Ni-N-C low sample

Figure S3a presents EELS mapping of C, N, O of the particle shown in **Fig. 2**

Section S7 Ni-N-C-high detailed analysis

S7A Ni-N-C-high detailed analysis of areas A1 and A1a

Figure S4 illustrates the conversion of measured transmission STXM images to the corresponding optical density (OD) images using the Beer-Lambert law:

$$OD(x,y) = -\ln(I(x,y) / I_o)$$

where I(x,y) is the transmitted intensity at pixel (x,y) and Io is the incident flux, measured off the sample, but through all other components of the STXM (all optics, windows, the sample support and the detector. **Fig. 3c** (main manuscript) presents the difference, $\Delta OD = OD_{852.7} - OD_{848}$, which is called a **stack map**. It is a map of the Ni content present in aggregate **A1**.

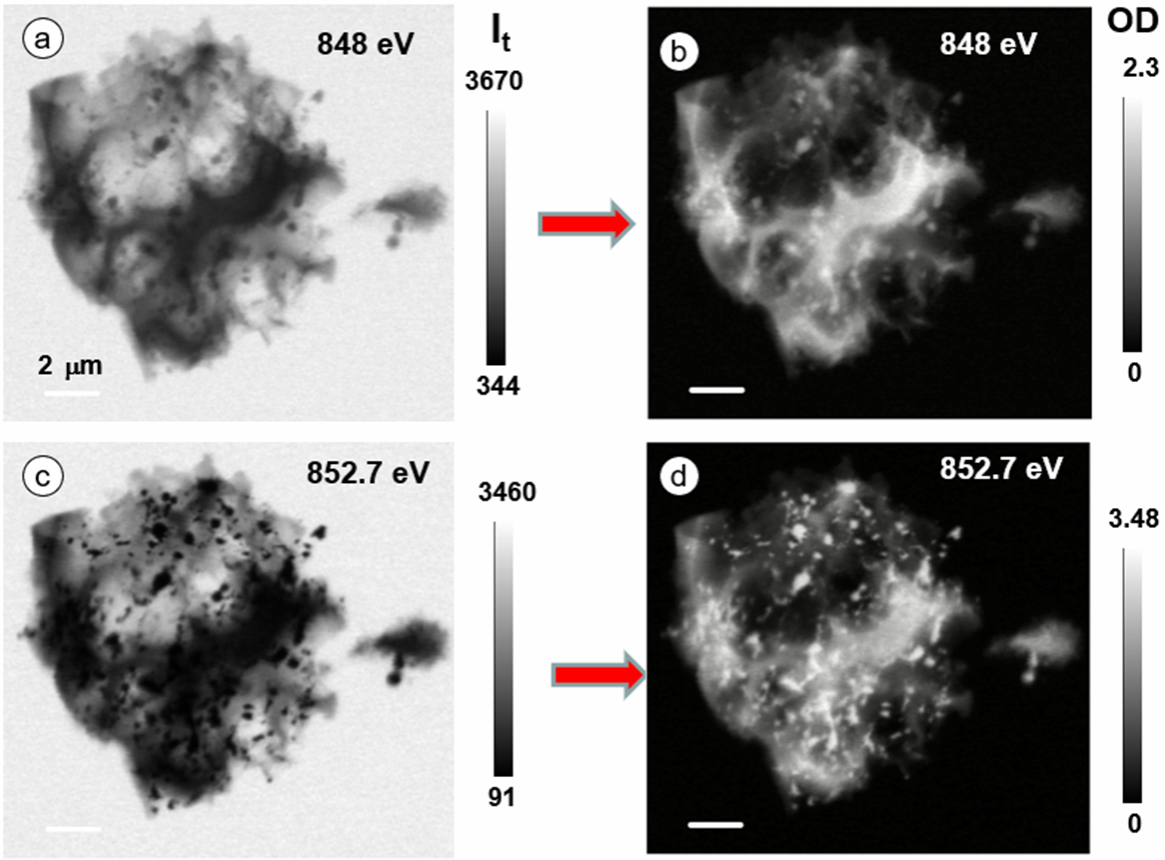

Figure S4 optical density (OD) conversion for region **A1** on SiNx window **a, b)** at 848 eV, **c, d)** at 852.7 eV.

Figure S5 compares the optimized Ni 2p spectra of the particles and matrix (i.e. from the masked regions in **Fig. 3e**) to the Ni 2p spectra of 7 reference compounds, which, from the perspective of the catalyst synthesis, are candidates for being present in the catalyst. Careful examination shows a good alignment of the low energy Ni $2p_{3/2}$ peak in the particle spectrum with the Ni $2p_{3/2}$ peak in Ni metal, the low energy Ni $2p_{3/2}$ peak in the matrix spectrum with the Ni $2p_{3/2}$ peak in Ni_3S_2 and the higher energy Ni $2p_{3/2}$ peak in the matrix spectrum with the Ni $2p_{3/2}$ peak in Ni-TPP. Corresponding alignments are also present in the Ni $2p_{1/2}$ spectral region. Based on these observations we explored the use of the spectra of Ni metal [Ni(0)], Ni-TPP and Ni_3S_2 to interpret the Ni 2p spectra of the catalysts studied, as presented in the paper.

Figure S6 summarizes the analysis of the Ni 2p stack of region **A1a** of the Ni-N-C-high sample using internal spectra extracted from the Ni 2p stack. While this does provide one possible interpretation of the data, it is not optimal because of the relatively high and structured residual, which suggests a third component may give an improved fit, the chemical identity is not defined and the analysis at this stage is only qualitative. In order to go further, it is useful to compare the optimized particle and matrix spectra with the Ni 2p spectra of possible species present.

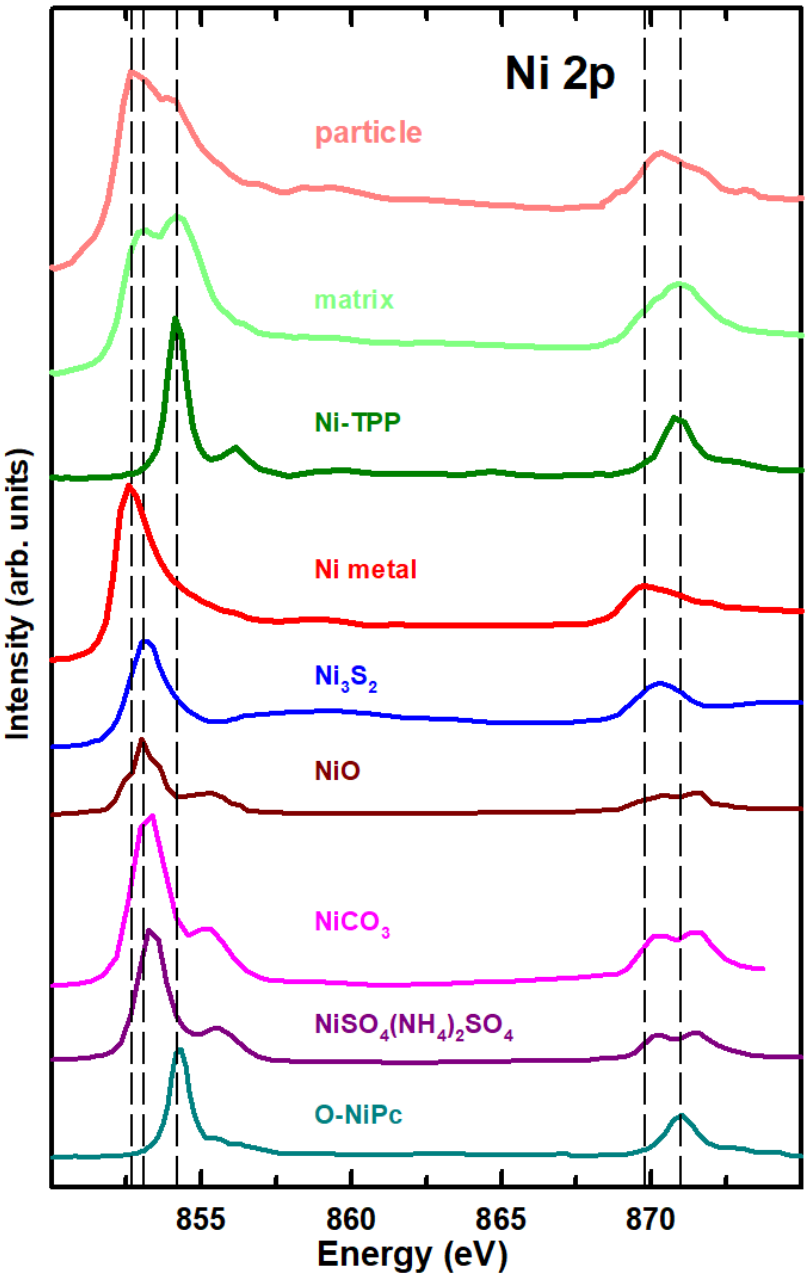

Figure S5 Optimized Ni 2p spectra of particles (light red) and matrix (light green) in region **A1a**, compared with reference spectra of NiTPP, Ni(0), Ni_3S_2, NiO, $NiCO_3$, Ni ammonium sulphate and O-NiPc. The vertical lines indicate correlation of positions in the Ni-C-N catalyst with features in the spectra of the reference compounds.

Figure S7 presents a verification of the analysis of the Ni 2p stack of region **A1a** of the Ni-N-C sample, as a linear combination of Ni(0), NiTPP and Ni_3S_2 components, as presented in **Fig. 4** of the paper. **Table S5** summarizes the quantitative results for this curve fit analysis.

Table S5 Results of SVD curve fit analysis of region **A1a** of the Ni-N-C sample

	Species (average thickness in nm)			
area	Ni(0)	Ni-TPP	Ni_3S_2	χ^2
Ni(0) region	29	160	2	0.06
NiTPP region	6	85	3	0.02
N_3S_2 region	7	90	31	0.02

Section S7B SVD analysis of Ni 2p stack of region A2 of Ni-N-C-high

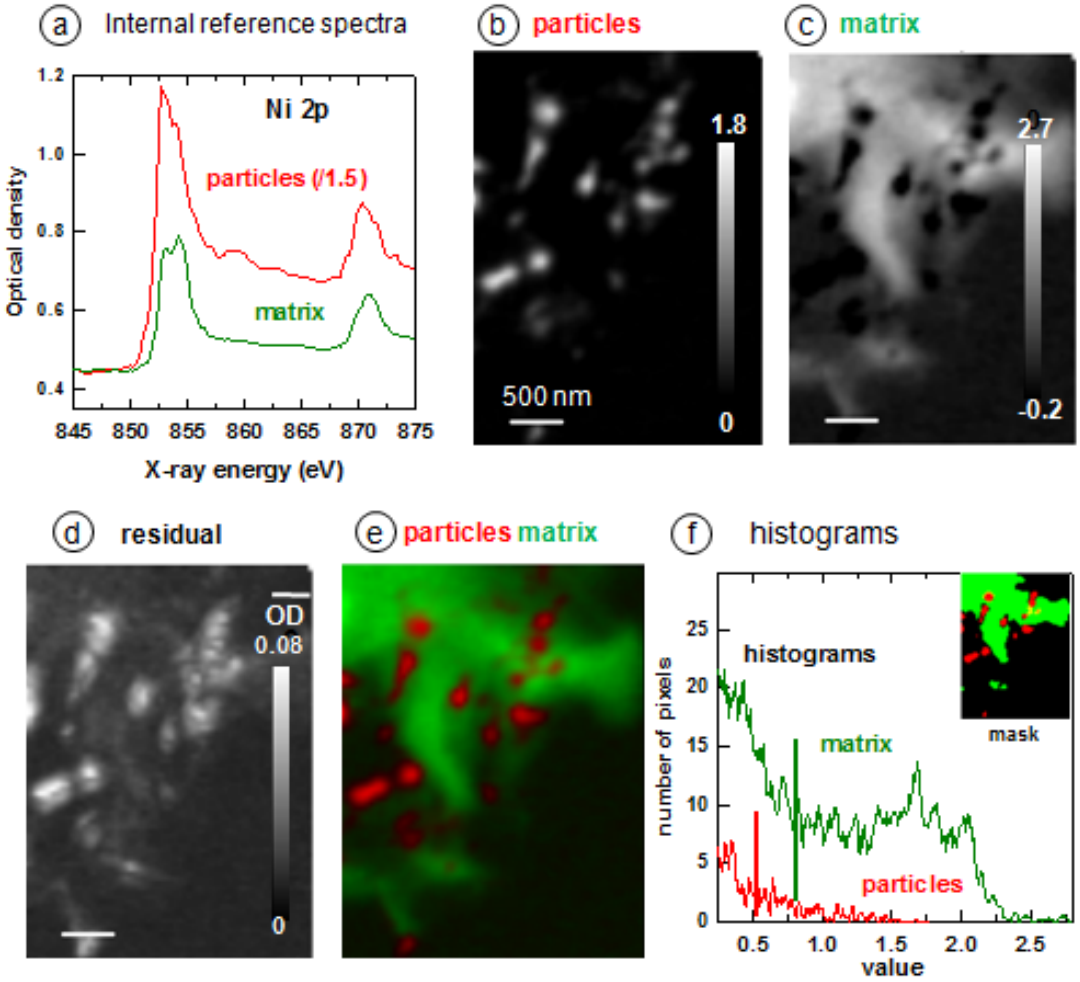

Figure S6 SVD analysis of the Ni 2p stack of region **A1a** of the Ni-N-C-high sample using internal reference spectra. **a)** Spectra of particles and matrix from arbitrarily selected areas. **b)** component map of the particles. **c)** component map of the matrix region. The grayscales in **(b, c)** are in multiplicative units of the reference spectra. **d)** residual of the fit. **e)** color coded composite of the particle (red, a) and matrix (green, b) maps. **f)** histogram of pixel values in the component maps. The vertical lines indicate the thresholds used. All pixels above these values form 0/1 masks (displayed as the insert) which is used to extract optimized spectra of the particles and matrix.

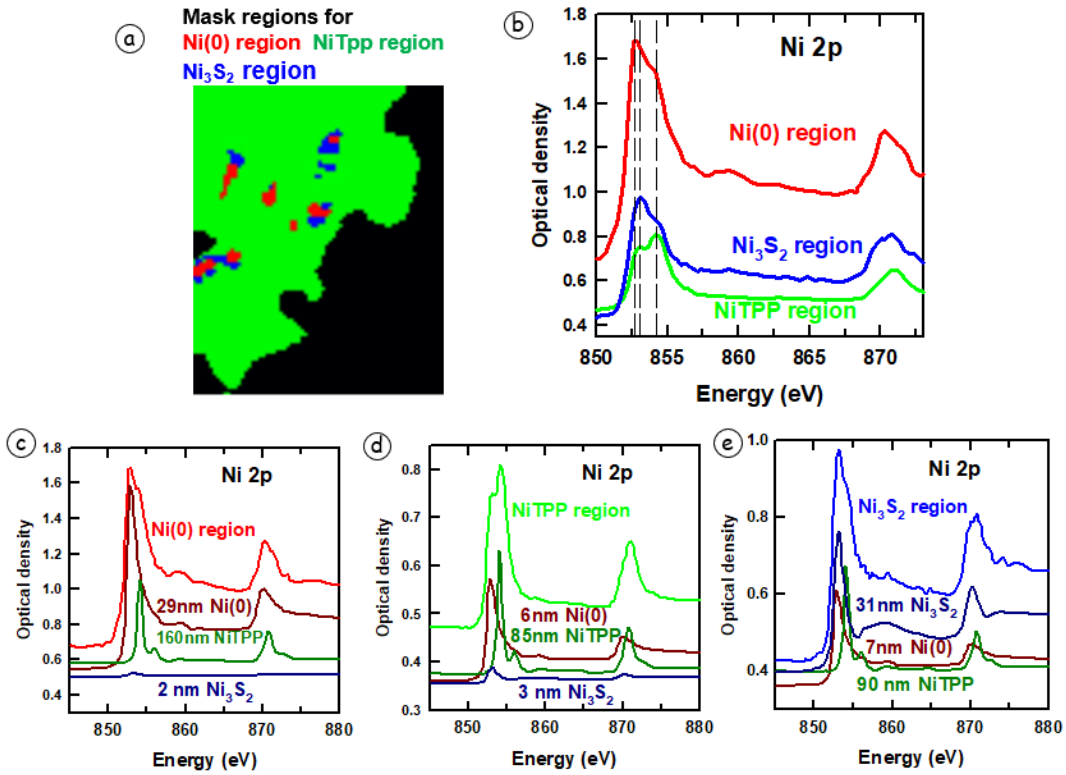

Figure S7 Spectral domain representation of the 3 component (Ni(0), NiTPP, Ni_3S_2) SVD analysis of the Ni 2p stack of region **A1a** of the Ni-C-N-high catalyst. **a)** shows the masked regions for Ni(0), NiTPP, Ni_3S_2. **b**) the internal spectra for the regions of Ni(0), NiTPP, Ni_3S_2. **(c)** curve fit of the Ni(0) region. **d**) curve fit of the NiTPP region. **e**) curve fit of the Ni_3S_2 region.

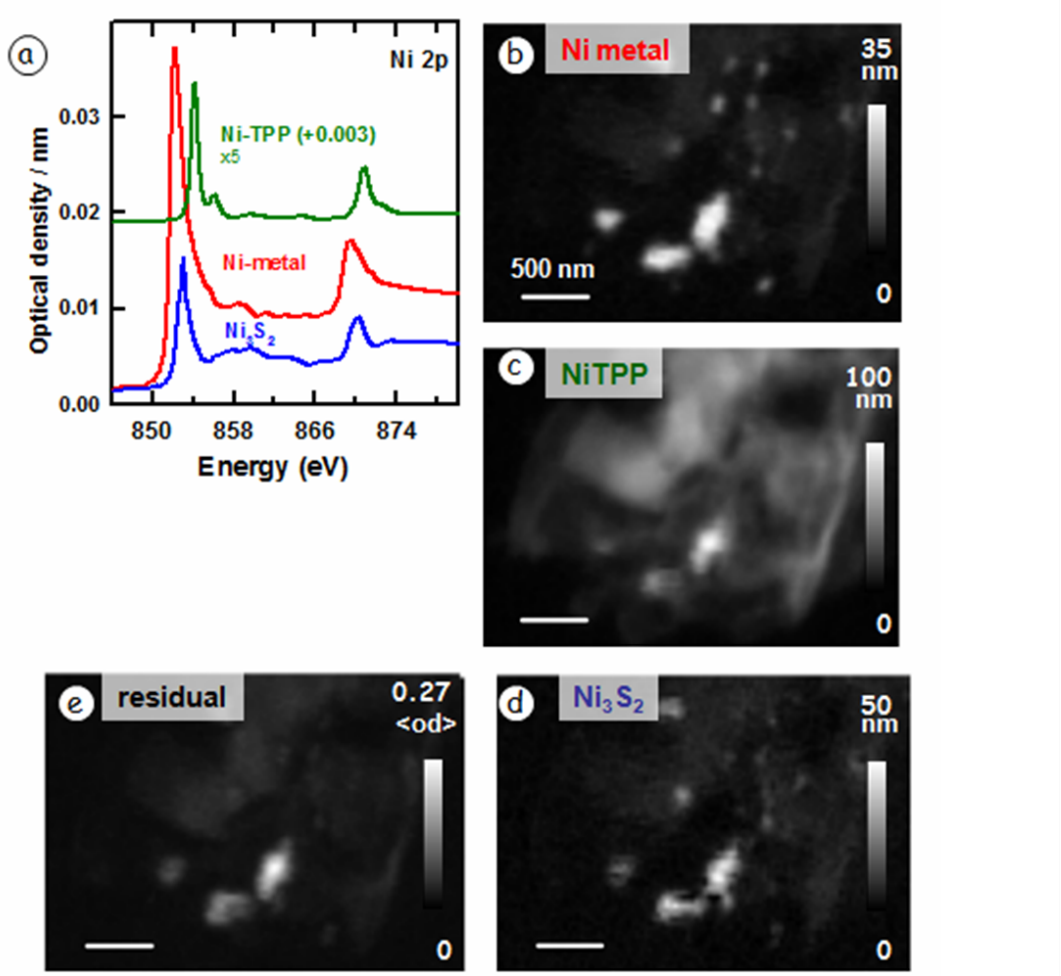

Figure S8 SVD analysis of Ni 2p stack of region **A2** of Ni-N-C-high. (**a**) OD1 spectra of Ni metal, Ni-TPP* and Ni_3S_2 used to fit the stack. The NiTPP reference spectrum is the OD1 spectrum of Ni-TPP with an additional 0.003 added, to account for the fraction of the matrix region which has C-N-O signal but not Ni 2p signal. **b)** component map of the Ni metal. **c)** component map of the Ni –TPP*. **d)** component map of Ni_3S_2. **e)** Residual of fit. See **Fig. 4b** for the color coded composite

Figure S8 presents the SVD analysis of Ni 2p stack of region **A2** of Ni-N-C-high using optical density per nm (OD1). In order to account for the significant part of the matrix where there is C-N-O but no Ni, a constant value of 0.003 was added to the OD1 spectrum of NiTPP, so that the relative proportions of pre-edge and Ni 2p signal were similar to that in the spectrum of the matrix.

Figure S9 presents verification of the analysis of the Ni 2p stack of region **A2** of the Ni-N-C sample, as a linear combination of Ni(0), Ni-TPP and Ni_3S_2 components . **Table S6** presents the numerical results.

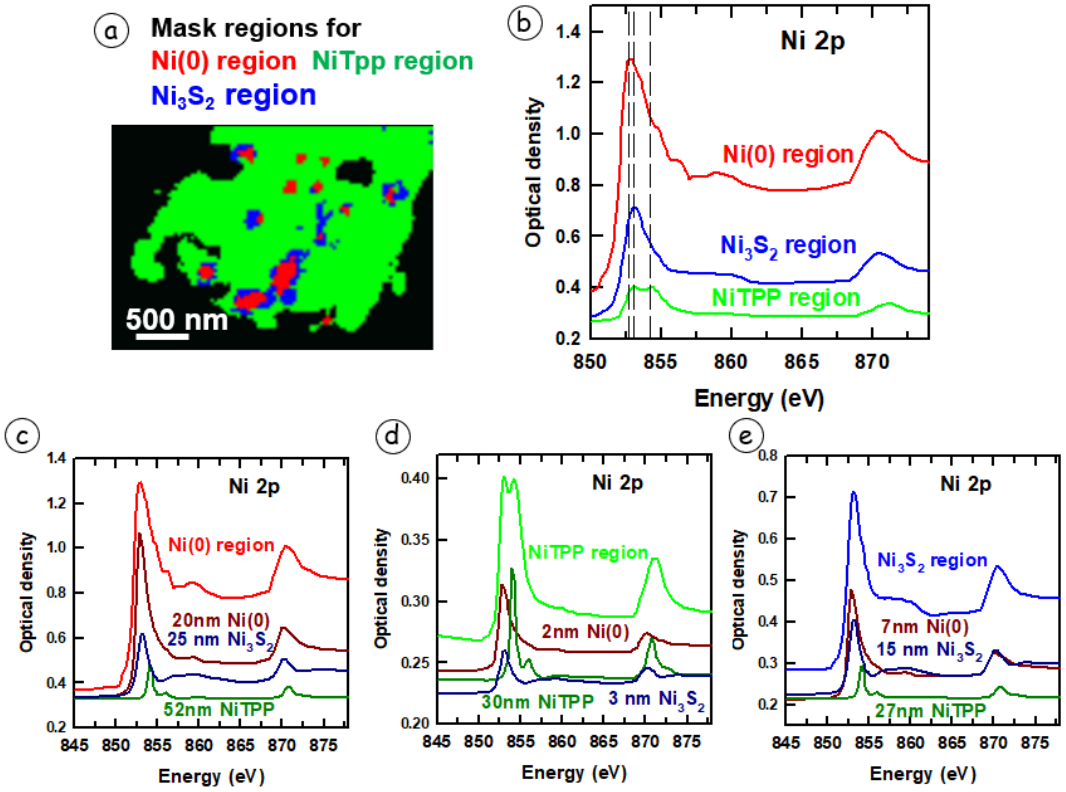

Figure S9 Spectral domain representation of the 3 component (Ni(0), NiTPP, Ni_3S_2) SVD analysis of the Ni 2p stack of region **A2** of the Ni-C-N-high catalyst. **a)** Masked regions the Ni(0) (red), NiTPP (green) and Ni_3S_2 (blue) regions. **b**) the internal spectra for the regions of Ni(0), NiTPP, Ni_3S_2 **c**) curve fit of the Ni(0) regions. **d**) curve fit of the NiTPP regions. **e**) curve fit of the Ni_3S_2 regions.

	Species (average thickness in nm)			
area	Ni(0)	Ni-TPP	Ni_3S_2	χ^2
Ni region	20	52	25	0.23
NiTPP region	2	30	3	0.03
N_3S_2 region	7	27	15	0.03

Table S6 Results of SVD curve fit analysis of region **A2** of the Ni-N-C sample

Section S8 O 1s and S 2p results for area A2 of the Ni-N-C-high sample.

Figure S10 present the O 1s and S 2p results for area **A2** of the Ni-N-C-high sample.

Section S9 Analysis of Ni 2p stack of region B1 of the Ni-N-C-low sample

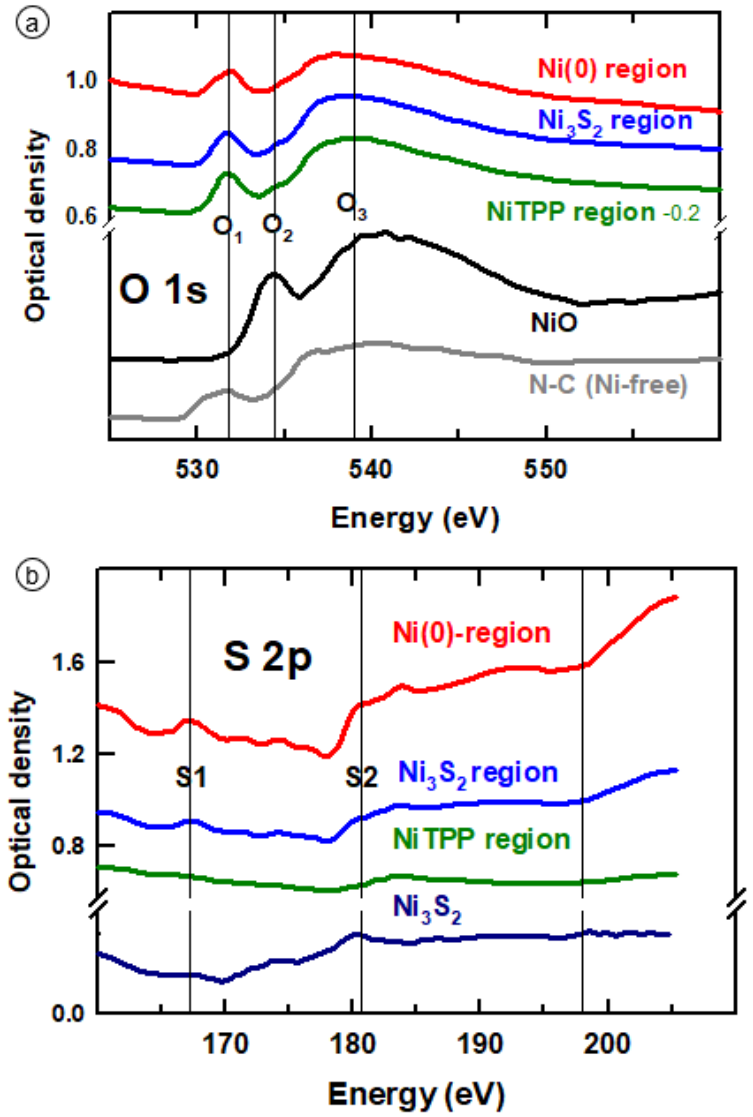

Figure S10 O 1s and S 2p results for area **A2** of the Ni-N-C-high sample. **a)** O 1s spectra of Ni(0) dominant, NiTPP dominant and Ni_3S_2 dominant areas from the O 1s stack of the **A2** region compared to the reference spectra of Ni(0), NiTPP and Ni_3S_2. **b)** S 2p spectra of Ni(0) dominant, NiTPP dominant and Ni_3S_2 dominant areas from the S 2p stack of the **A2** region

Figure S11 presents the results of an SVD analysis of Ni 2p stack of region **B1** of the Ni-N-C-low sample.

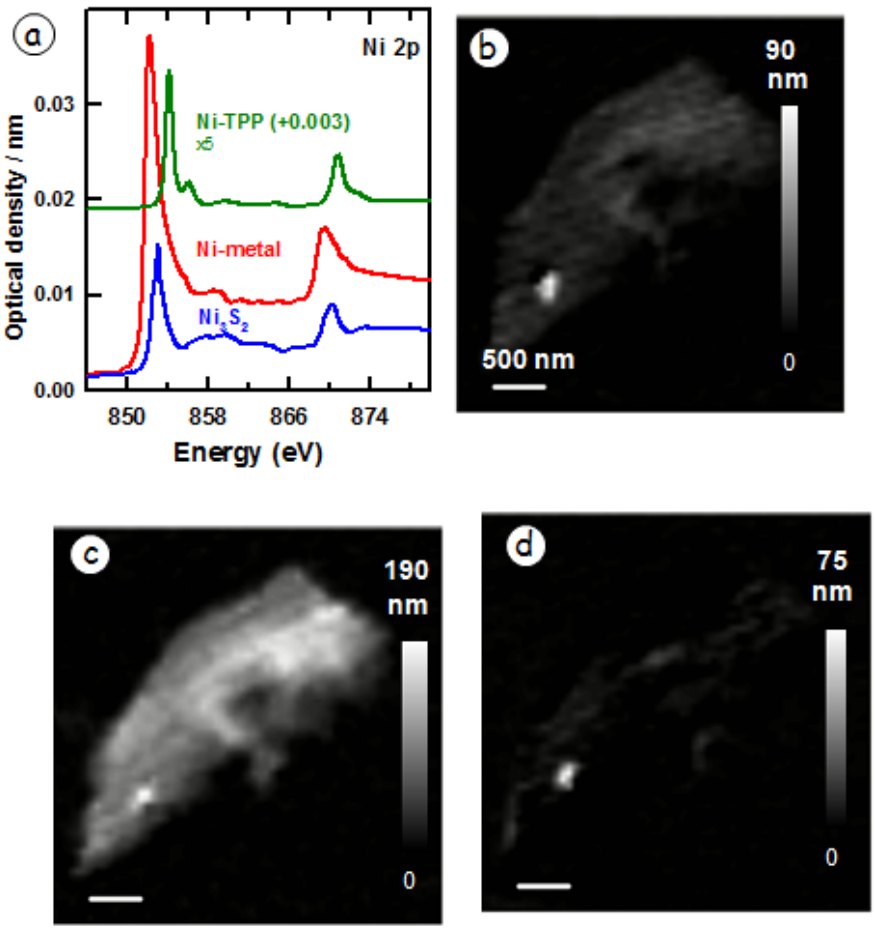

Figure S11 SVD analysis of Ni 2p stack of region **B1** of Ni-N-C low. (**a**) OD1 spectra of Ni metal, Ni-TPP* and Ni_3S_2 used to fit the stack. The NiTPP reference spectrum is the OD1 spectrum of Ni-TPP with an additional 0.003 added, to account for the fraction of the matrix region which has C-N-O signal but not Ni 2p signal. **b)** component map of the Ni metal. **c)** component map of the NiTPP. **d)** component map of Ni_3S_2. **e)** Residual of fit. See **Fig. 6b** for the color coded composite of these

Figure S12 presents a spectral domain check on the SVD analysis of the Ni 2p stack of region **B1** of Ni-N-C low.

Section S10 Analysis of all edges of region B1 of the Ni-low sample.

Figure S13 presents the combined Ni 2p, O 1s, C 1s and O 1s spectra data for the region **B1** of the Ni-C-N-low catalyst. Should be mentioned that some area in B1 was absorption saturation at the N 1s edge. The N 1s spectra shown in Fig.S22-c was adjusted according to N 1s spectra of the un-saturation area in B1 region.

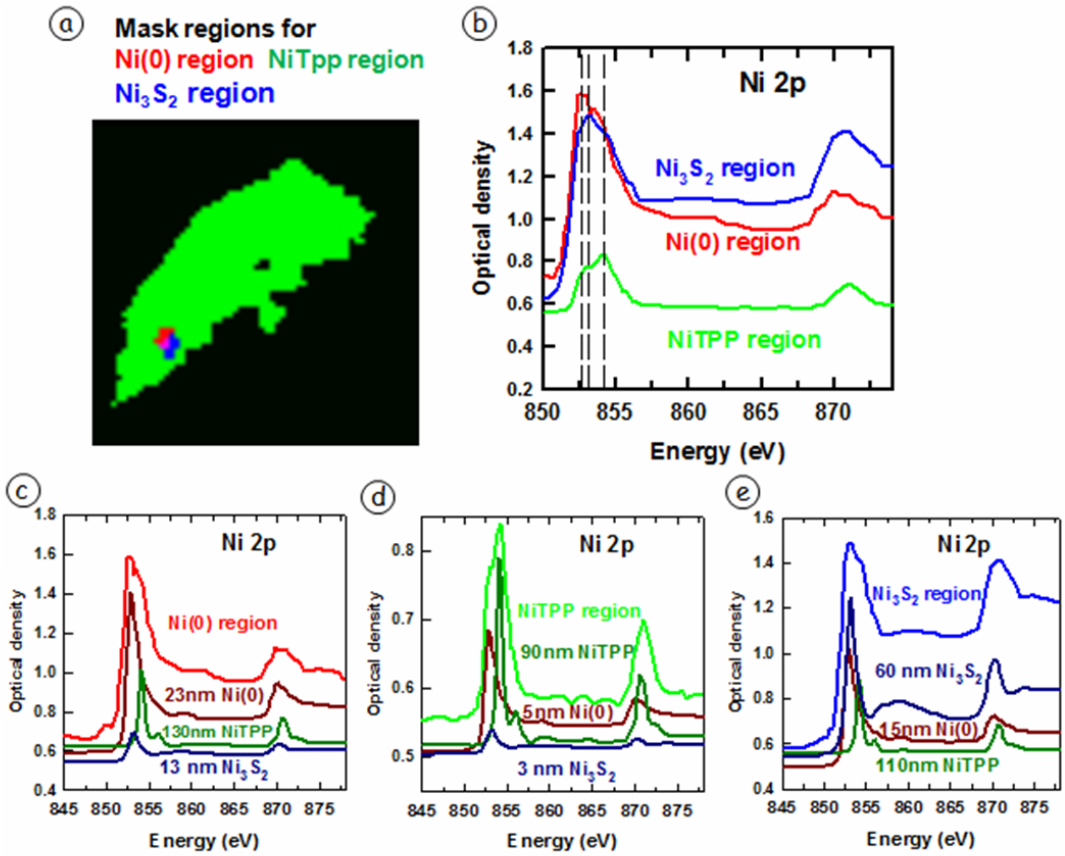

Fig. S12 Spectral domain representation of the 3 component (Ni(0), NiTPP, Ni_3S_2) SVD analysis of the Ni 2p stack of region **B1** of the Ni-C-N-low catalyst. **a)** Masked regions the Ni(0) region (red), NiTPP region (green) and Ni_3S_2 region (blue). **b**) the internal spectra for the regions of Ni(0), NiTPP, Ni_3S_2 **c**) SVD curve fit of the Ni(0) region. **d**) SVD curve fit of the NiTPP region. **e**) SVD curve fit of the Ni_3S_2 region.

Section S11 Analysis of other regions of the Ni-N-C high sample

Figure S14 presents a summary of the Ni 2p analysis of all the regions of Ni-N-C-high sample studied (**A1a-A5**) Mole fractions of Ni(0), NiTPP, Ni_3S_2 and amounts of carbon in 5 different particles of the Ni-N-C-high catalyst sample. Rescaled color coded composites of the component maps from analysis of Ni 2p stacks of each region are indicated.

Section S12 Analysis of other regions of the Ni-N-C-low sample

Figure S15 presents a summary of the Ni 2p analysis of all the regions of Ni-N-C-low sample **B1-B4**. **(b)** Mole fractions of Ni(0), NiTPP, Ni_3S_2 and amounts of carbon in 5 different particles of the Ni-N-C-low catalyst sample. Rescaled color coded composites of the component maps from analysis of Ni 2p stacks of each region are indicated.

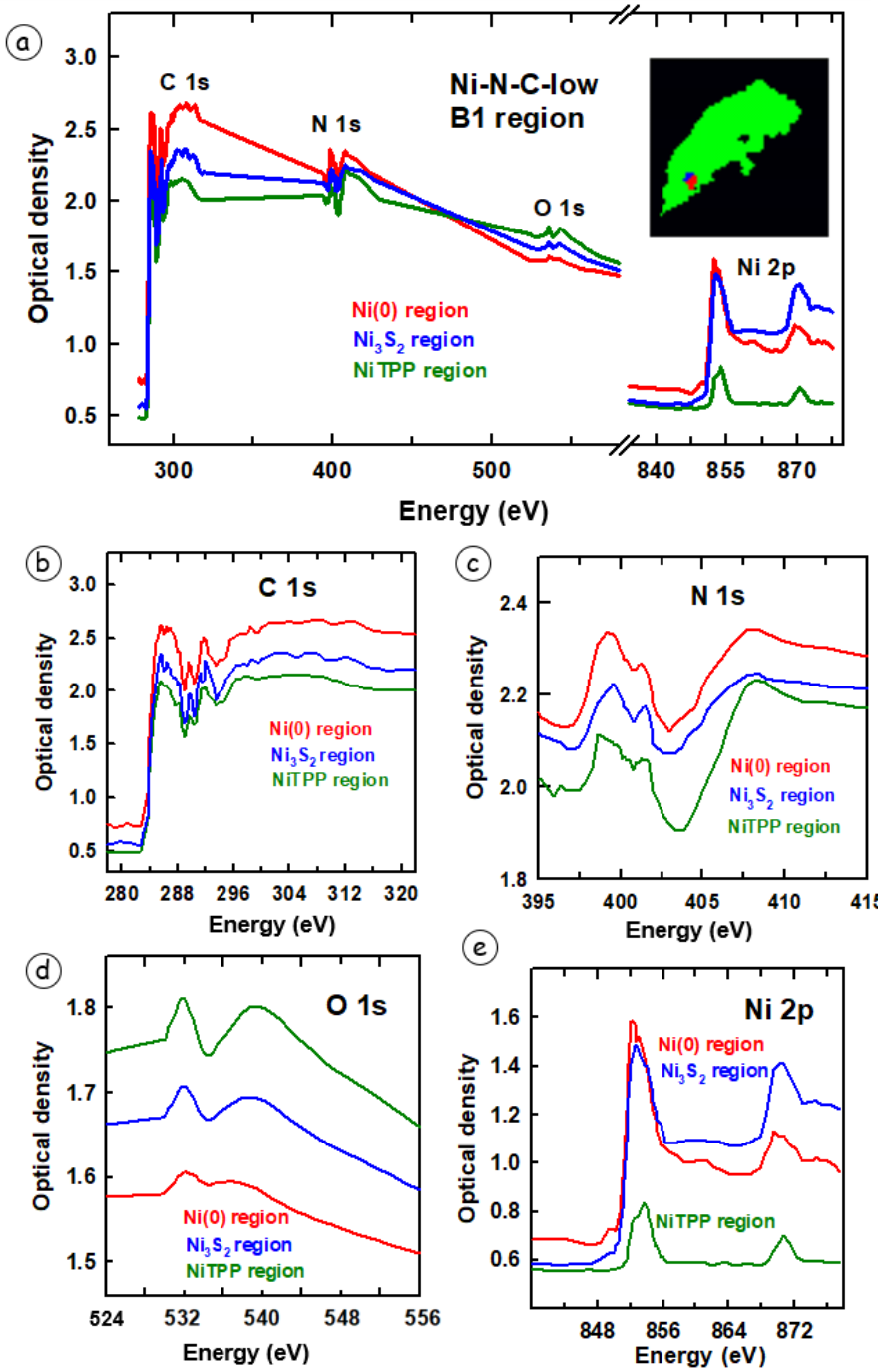

Fig. S13 a) the spectra for a) Ni 2p, N 1s, O 1s, C1s edge of extraction area for regions of Ni(0) (red), NiTPP (green) and Ni_3S_2 (blue). **Insert**: the color coded (rescaled) composite of extraction area for dominant Ni(0) (red), NiTPP (green) and Ni_3S_2 (blue) in region **B1**. The spectra of **b)** Ni 2p **c)** N 1s, **d)** C 1s, **e)** O 1s at the regions of Ni(0) (red), NiTPP (green) and Ni_3S_2 (blue).

Section S13 Quantitative results from STXM analysis of the Ni-high and Ni-low samples

Table S7 presents the results of the curve fit to the average Ni 2p spectra of regions **A1-A5** of the Ni-N-C-high sample and **B1-B4** of the Ni-N-C-low sample.

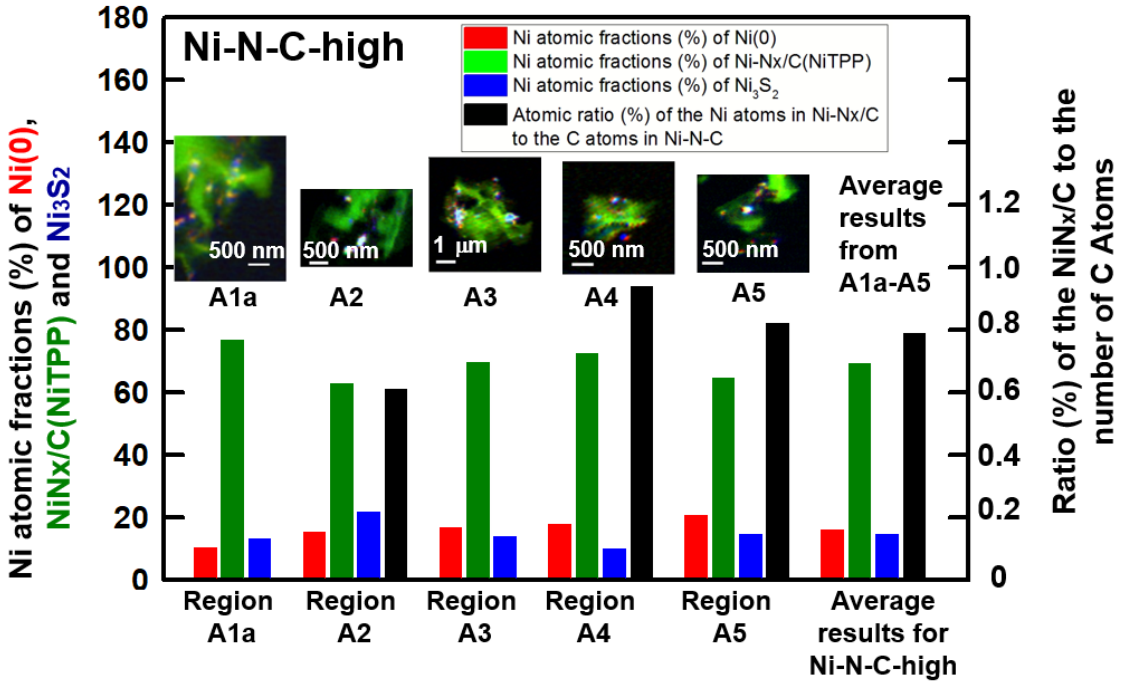

Fig. S14 Overview of analyses of regions **A1a, A2, A3, A4**, and **A5** of the Ni-N-C-high sample

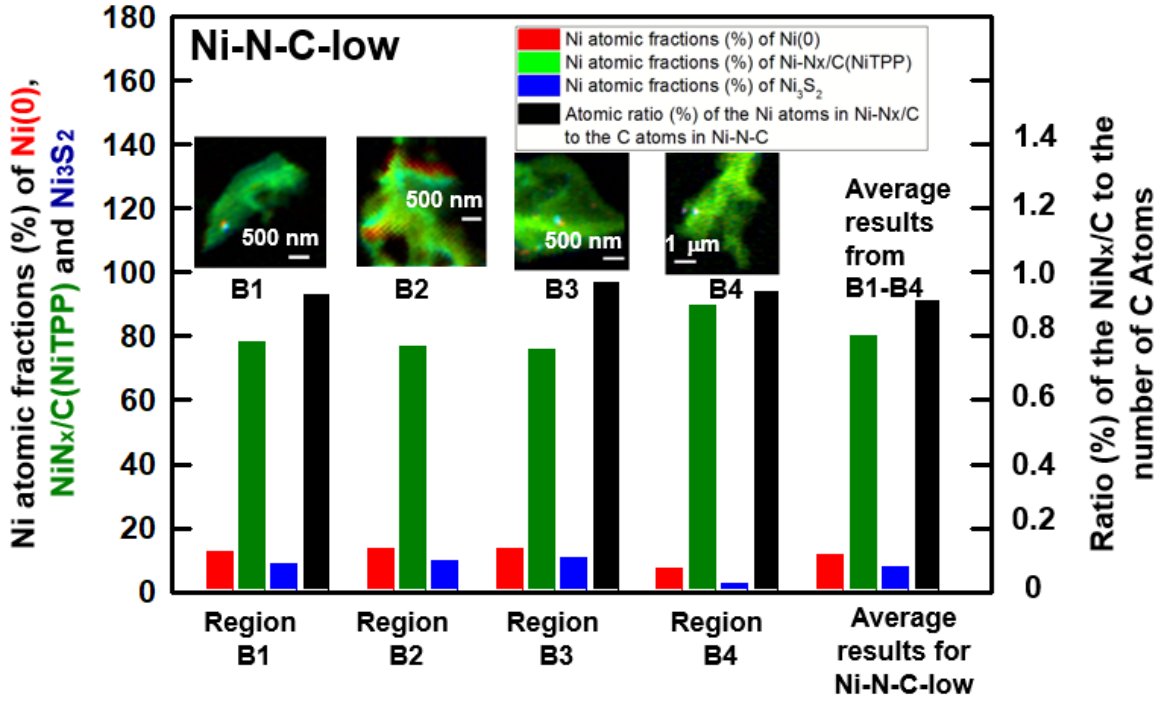

Fig. S15 Overview of analysis of regions **B1, B2, B3**, and **B4** of the Ni-N-C-low sample

Sample	Sample region	Area of extraction (um2)	Calculation from the Ni 2p STXM stacks															Calculation from the C 1s STXM stacks			Atomic ratio of the Ni atoms in NiN_xC to the C atoms in the Ni-N-C samples
			Volume of Ni species (um3)				Mass of Ni species (10^-15 g)				Mol of Ni atoms in each Ni species (10^-15 mol)				Ni atomic fractions in each Ni species			Volume of graphite carbon (um3)	Weight of graphite carbon (10^-15 g)	Mol of carbon atoms (10^-15 mol)	
			Ni(0)	NiTPP	Ni_3S_2	Total	Ni(0)	NiTPP	Ni_3S_2	Total	Ni(0)	NiN_xC (NiTPP)	Ni_3S_2	Total	Ni(0)	NiN_xC (NiTPP)	Ni_3S_2				
Ni-N-C-high	A1a	38.44	0.22	3.6	0.26	4.1	25.0	2256.0	44.4	2325.4	0.43	3.2	0.56	4.2	**10%**	**77%**	**13%**	-	-	-	**-**
	A2	18.49	0.072	0.63	0.091	0.80	8.10	396.4	15.6	420.10	0.14	0.56	0.20	0.90	**15%**	**63%**	**22%**	2.53	1118.4	93.2	**0.61%**
	A3	144	1.4	12.7	1.1	15.2	158	7947	181.2	8286.8	2.7	11.3	2.3	16.3	**16%**	**70%**	**14%**	-	-	-	**-**
	A4	1.21	0.005	0.046	0.0025	0.54	0.58	28.6	0.44	29.6	0.01	0.04	0.005	0.06	**18%**	**72%**	**10%**	0.12	52.2	4.4	**0.94%**
	A5	7.29	0.026	0.17	0.016	0.21	2.9	107.5	2.8	113.2	0.05	0.15	0.035	0.24	**21%**	**65%**	**14%**	0.51	224.8	18.7	**0.82%**
	Average Ni-N-C-high	-	-	-	-	-	-	-	-	-	-	-	-	-	**16%**	**69%**	**15%**	-	-	-	**0.79%**
Ni-N-C-low	B1	16.81	0.087	1.2	0.055	1.3	9.8	935.4	9.6	754.8	0.17	1.1	0.12	1.3	**12%**	**79%**	**9%**	3.0	1338.9	111.6	**0.93%**
	B2	53.29	0.25	3.0	0.15	3.4	27.5	1881.8	26.6	1936.0	0.47	2.7	0.33	3.5	**13%**	**77%**	**10%**	-	-	-	**-**
	B3	30.25	0.19	2.3	0.14	2.6	21.4	1442.5	23.5	1487.4	0.36	2.1	0.29	2.7	**13%**	**76%**	**11%**	5.7	2520.4	210.0	**0.97%**
	B4	169	0.42	10.9	0.14	11.4	47.5	6791.7	23.3	6862.5	0.81	9.7	0.29	10.8	**7%**	**90%**	**3%**	31.3	13847.1	1152.8	**0.84%**
	Average Ni-N-C-low	-	-	-	-	-	-	-	-	-	-	-	-	-	**12%**	**80%**	**8%**				**0.91%**

Table S7 Quantitative results from curve fits of the Ni(0), Ni_3S_2 and NiTPP reference spectra to the average Ni 2p spectra of regions **A1-A5** of the Ni-N-C-high sample and **B1-B4** of the Ni-N-C-low sample.

Section S14A Total electron yield (TEY) XAS measurements

Figure S16 presents the results of total electron yield (TEY) X-ray absorption spectroscopy (XAS) measurements for the Ni-N-C-high, -N-C-low samples and other reference samples at the Ni 2p, N 1s and C 1s edges. In general, there is good agreement between the shapes of the TEY spectra and the OD spectra measured with STXM.

Section S14B Comparison of XAS and STXM from Ni 2p, C1s and N 1s

To compare the capabilities of STXM to study catalysts on a single particle basis, with ensemble-averaged characterization techniques, X-ray absorption spectra (XAS) were collected at the Ni 2p, C1s and N 1s edges using TEY detection at the CLS SGM beamline. XAS (**Fig. S16**) and STXM (**Fig. 4b, 5d, 5e and Fig. S5)** spectra of the pure, homogeneous reference compounds are almost identical. The TEY-XAS and STXM Ni 2p spectra of the highly heterogeneous Ni-N-C materials are displayed in **Fig. S17a** for Ni-N-C-high and **Fig. S17b** for Ni-N-C-low. Overall, the Ni 2p spectra collected by TEY-XAS and STXM are very similar, indicating that STXM is capable of collecting spectral information from a single particle that is reflective of the spectral information collected by TEY-XAS averaged over several thousand particles. The only discrepancy between the two techniques is for the Ni-N-C-high sample (**Fig. S17a**). While the shape and location of peaks in the TEY-XAS and STXM spectra are the same, the intensities of the peaks at 852.7 eV (Ni(0)) and 853.1 eV (Ni_3S_2) are higher in the TEY-XAS than the STXM spectra. The relative amounts of Ni(0), NiTPP and Ni_3S_2 in the Ni-N-C-high and Ni-N-C-low samples were determined by curve fitting the TEY-XAS spectra to the quantitative OD1 reference spectra

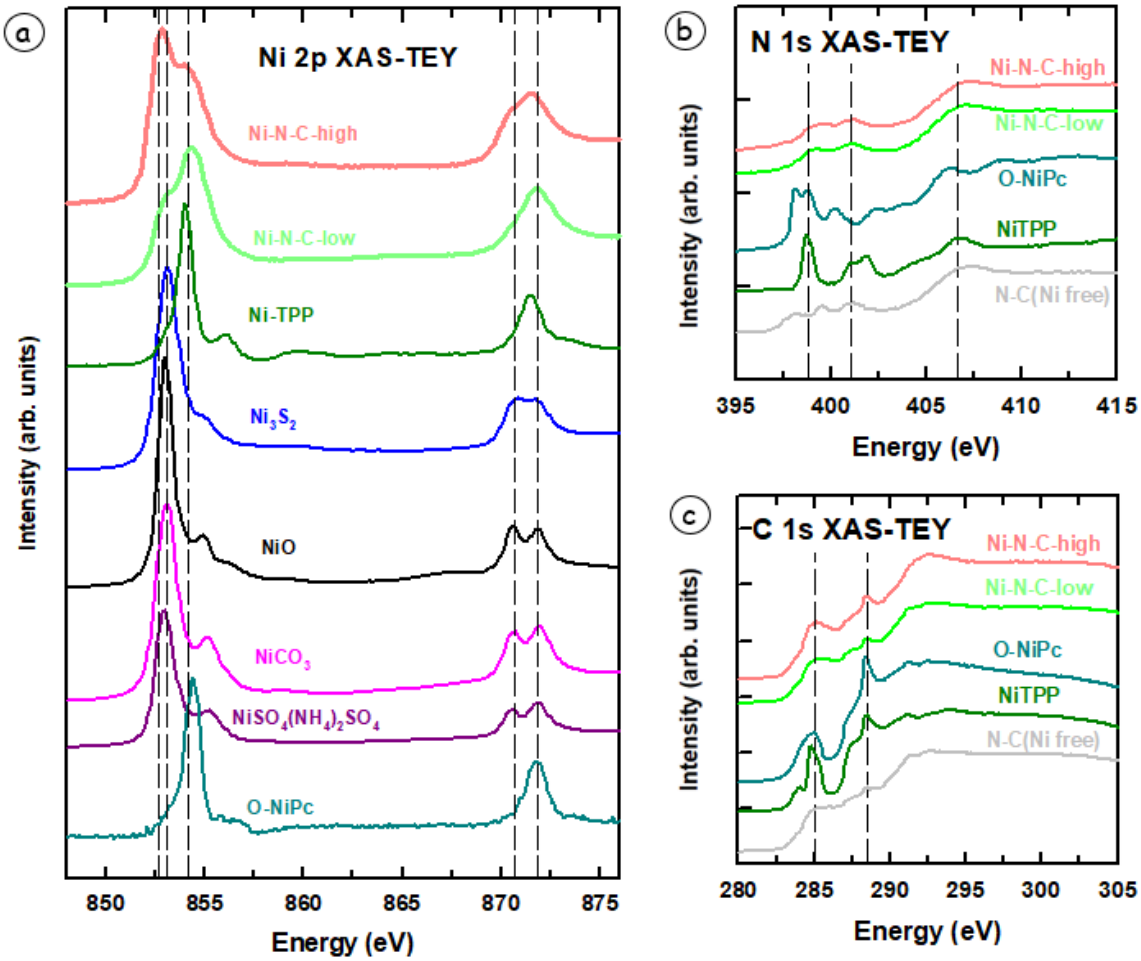

Fig. S16 Total electron yield (TEY) X-ray absorption spectroscopy (XAS) measurements for the Ni-N-C-high, -N-C-low samples and other reference samples at **a)** Ni 2p, **b)** N 1s and **c)** C 1s edge.

shown in **Fig. 4b**. The fraction of the Ni atoms present in each domain was calculated and reported in **Table S8**. The quantitative composition results for STXM and TEY-XAS are presented in **Fig. S18**. The somewhat larger amount of Ni(0) found in the STXM results for Ni-N-C-high is probably due to the need to select relatively thin regions without thick Ni(0)/ Ni_3S_2 particles to avoid absorption saturation (such as the selection of **A1a** region in **A1**). Note that the XAS results cannot be used to calculate the 'Absolute Ratio (%) of NiN_x/C Sites' because the C 1s signal from TEY-XAS is not from the same thickness as the Ni 2p signal due to different electron escape depths.

Figure S17 compares the XAS-TEY and STXM Ni 2p spectra of the Ni-N-C materials. There is good agreement between the shapes of the XAS-TEY spectra and the OD spectra measured with STXM.The similarity of the TEY-XAS and STXM results confirms that, despite measuring an extremely small

volume, STXM can measure the average properties of heterogeneous materials. However, a key advantage of STXM is that it probes the chemistry of individual catalyst particles with sub-50 nm spatial resolution, even when the species of interest (i.e., NiN_x/C) contribute only a portion of the overall spectral features. For example, consider the Ni-N-C-high data shown in **Fig. S17a.** When interpreting the TEY-XAS data, the Ni_3S_2 contribution at 853.1 eV could be easily overlooked in an ensemble averaged XAS study as it is largely overshadowed by the neighboring Ni(0) peak at 852.7 eV. On the contrary, with the spatial resolution of STXM it is possible to identify and differentiate these individual chemical species, which allows for mapping of their chemical signals and distributions throughout the catalyst structure.

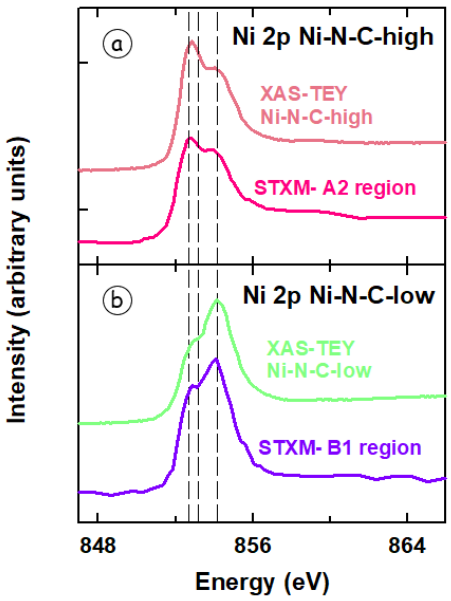

Fig. S17 Comparison for XAS and STXM results of Ni-N-C materials at Ni 2p edge. (a) Ni 2p XAS-TEY spectra of the Ni-N-C-high sample compared with the average STXM spectra of the Ni-N-C-high sample (**A2**). **(b)** Ni 2p XAS-TEY spectra of the Ni-N-C-low sample compared with the average STXM spectra of the Ni-N-C-low sample (**B1**). The dashed lines are the positions of the main $2p_{3/2} \rightarrow 3d$ peaks of Ni(0) at 852.7 eV, Ni3S2 at 853.1 eV, and NiN_x/C at 854.2eV. The intensities of each spectrum are scaled so the difference in signals ate 864 eV and 848 are the same for each data set. Offsets are used for clarity.

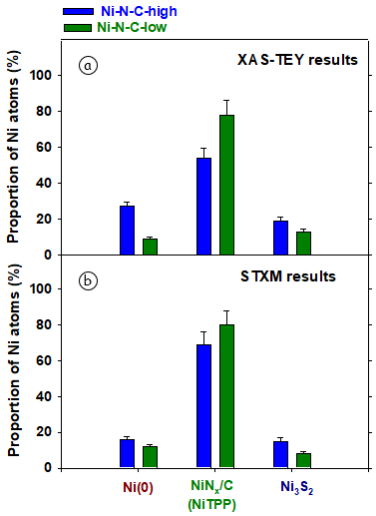

Fig. S18 Group bar chart representing the quantitative distribution of different Ni-sites of the Ni-N-C-high and Ni-N-C-low sample from (a) XAS-TEY results and (b) STXM results. Represents the total proportion of Ni atoms (out of all the Ni atoms in the sample) present in the configuration shown on the x-axis for both catalysts investigated.

After using Ni 2p STXM stacks to characterize the spatial distribution of specific species, stacks at other edges can be measured over the same area, thereby gaining a more complete understanding of the chemical properties and how they vary throughout the catalyst (e.g., **Fig. 5** and **Fig. S13**). More importantly, based on this comprehensive understanding, enabled by location-dependent spectral interpretation, the amount of various chemical species present in the catalysts can be quantified (e.g. **Fig. 7, Fig. S14, S15**). Achieving this level of insight is not possible using ensemble averaged measurements such as X-ray absorption spectroscopy with limited or no spatial resolution. This comparison demonstrates the significant advantage of STXM for generating fundamental insight into catalyst structures and properties that are essential for guiding advanced material designs. Individual particles are measured with STXM, whereas the Ni 2p TEY-XAS spectra are measured over a 250 μm x 250 μm area spanning many thousands of particles of different sizes, frequently overlapping.

Table S8 presents numerical results from a compositional analysis of the XAS-TEY spectra of the Ni-N-C-high and Ni-N-C-low samples. The reference spectra for the fitting were those presented in **Fig. 4b. Figure S18** presents a group bar chart representing the quantitative distribution of different Ni-sites of the Ni-N-C-high and Ni-N-C-low sample calculated from XAS-TEY results.

Ni species (fraction of total signal)

sample	Ni(0)	NiTPP	Ni3S2
Ni-N-C-high	27%	54%	19%
Ni-N-C-low	9%	78%	13%

Table S8 Results of SVD curve fit analysis of XAS-TEY of the Ni-N-C samples

Section S15 Ptychography image of area A2 of the Ni-N-C-high sample

Figure S19a presents the ptychography amplitude image of area **A2** of the Ni-N-C-high sample at 852.7 eV, while **Fig. S19b** is an estimation of a spatial resolution of 10 nm (half pitch) from a Fourier ring correlation (FRC) analysis.

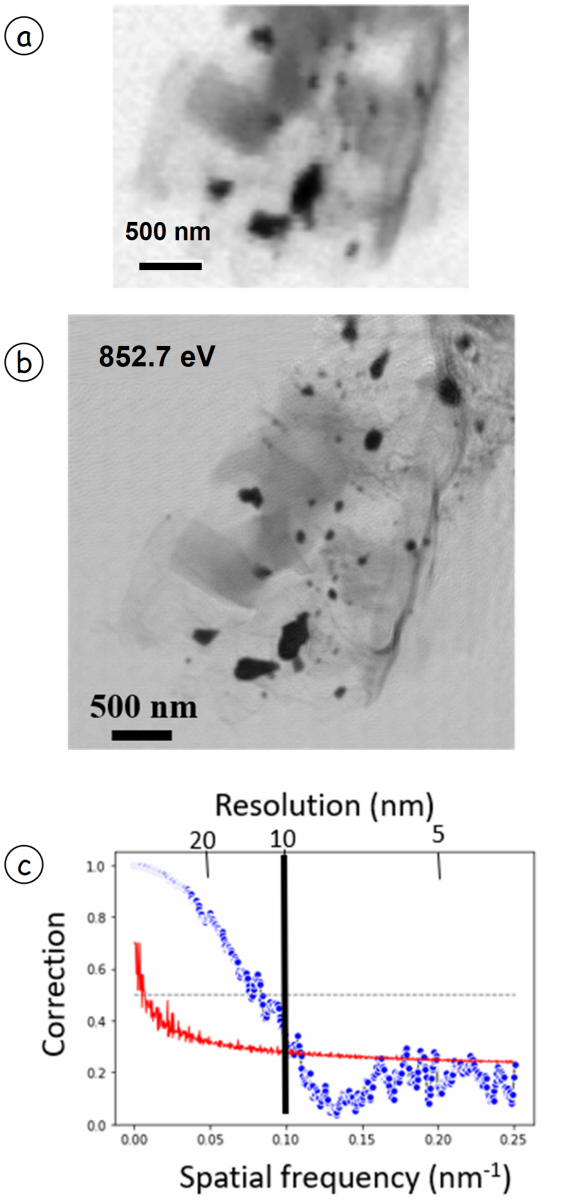

Figure S19 a) STXM images of region **A2** of the Ni-n-C high sample. **b)** Ptychography amplitude image of the Ni-N-C-high at A2 at 852.7 eV **c)** spatial resolution estimated from a Fourier ring correlation (FRC) analysis.

References

1. Lefèvre, M.; Dodelet, J. P.; Bertrand, P. O_2 Reduction in PEM Fuel Cells: Activity and Active Site Structural Information for Catalysts Obtained by the Pyrolysis at High Temperature of Fe Precursors. *J. Phys. Chem. B* **2000**, *104*, 11238–11247.
2. Lefèvre, M.; Dodelet, J. P.; Bertrand, P. Molecular Oxygen Reduction in PEM Fuel Cells: Evidence for the Simultaneous Presence of Two Active Sites in Fe-Based Catalysts. *J. Phys. Chem. B* **2002**, *106*, 8705–8713.
3. Zhao, S.; Cheng, Y.; Veder, J.-P.; Johannessen, B.; Saunders, M.; Zhang, L.; Liu, C.; Chisholm, M. F.; De Marco, R.; Liu, J.; Yang, S.-Z.; Jiang, S. P. One-Pot Pyrolysis Method to Fabricate Carbon Nanotube Supported Ni Single-Atom Catalysts with Ultrahigh Loading. *ACS Appl. Energy Mater.* **2018**, *1*, 5286–5297.
4. Wang, C.; Zhang, H.; Wang, J.; Zhao, Z.; Wang, J.; Zhang, Y.; Cheng, M.; Zhao, H.; Wang, J. Atomic Fe Embedded in Carbon Nanoshells–Graphene Nanomeshes with Enhanced Oxygen Reduction Reaction Performance. *Chem. Mater.* **2017**, *29*, 9915–9922.
5. Tylus, U.; Jia, Q.; Strickland, K.; Ramaswamy, N.; Serov, A.; Atanassov, P.; Mukerjee, S. Elucidating Oxygen Reduction Active Sites in Pyrolyzed Metal–Nitrogen Coordinated Non-Precious-Metal Electrocatalyst Systems. *J. Phys. Chem. C* **2014**, *118*, 8999–9008.
6. Jia, Q.; Ramaswamy, N.; Hafiz, H.; Tylus, U.; Strickland, K.; Wu, G.; Barbiellini, B.; Bansil, A.; Holby, E. F.; Zelenay, P.; Mukerjee, S. Experimental Observation of Redox-Induced Fe–N Switching Behavior as a Determinant Role for Oxygen Reduction Activity. *ACS Nano* **2015**, *9*, 12496–12505.
7. Koshy, D. M.; Chen, S.; Lee, D. U.; Stevens, M. B.; Abdellah, A. M.; Dull, S. M.; Chen, G.; Nordlund, D.; Gallo, A.; Hahn, C.; Higgins, D. C.; Bao, Z.; Jaramillo, T. F. Understanding the Origin of Highly Selective CO_2 Electroreduction to CO on Ni,N-Doped Carbon Catalysts. *Angewandte Chemie International Edition* **2020**, *59*, 4043–4050.
8. Whitby, J. A.; Östlund, F.; Horvath, P.; Gabureac, M.; Riesterer, J. L.; Utke, I.; Hohl, M.; Sedláček, L.; Jiruše, J.; Friedli, V.; Bechelany, M.; Michler, J. High Spatial Resolution Time-of-Flight Secondary Ion Mass Spectrometry for the Masses: A Novel Orthogonal ToF FIB-SIMS Instrument with In Situ AFM. *Advances in Materials Science and Engineering* **2011**, *2012*, e180437.
9. Shahcheraghi, L.; Zhang, C.; Lee, H.-J.; Cusack-Striepe, M.; Ismail, F.; Abdellah, A.; Higgins, D. C. Identifying Activity and Selectivity Trends for the Electrosynthesis of Hydrogen Peroxide via Oxygen Reduction on Nickel–Nitrogen–Carbon Catalysts. *J. Phys. Chem. C* **2021**, *125*, 15830–15840.
10. S. Sodhi, R. N. Time-of-Flight Secondary Ion Mass Spectrometry (TOF-SIMS) —Versatility in Chemical and Imaging Surface Analysis. *Analyst* **2004**, *129*, 483–487.
11. Lee, S. H.; Lin, J. C.; Farmand, M.; Landers, A. T.; Feaster, J. T.; Avilés Acosta, J. E.; Beeman, J. W.; Ye, Y.; Yano, J.; Mehta, A.; Davis, R. C.; Jaramillo, T. F.; Hahn, C.; Drisdell, W. S. Oxidation State and Surface Reconstruction of Cu under CO_2 Reduction Conditions from In Situ X-Ray Characterization. *J.*

Am. Chem. Soc. **2021**, *143*, 588–592.

12. Liu, L.; Corma, A. Identification of the Active Sites in Supported Subnanometric Metal Catalysts. *Nat Catal* **2021**, *4*, 453–456.
13. Chung, H. T.; Cullen, D. A.; Higgins, D.; Sneed, B. T.; Holby, E. F.; More, K. L.; Zelenay, P. Direct Atomic-Level Insight into the Active Sites of a High-Performance PGM-Free ORR Catalyst. *Science* **2017**, *357*, 479–484.
14. Koshy, D. M.; Landers, A. T.; Cullen, D. A.; Ievlev, A. V.; Meyer III, H. M.; Hahn, C.; Bao, Z.; Jaramillo, T. F. Direct Characterization of Atomically Dispersed Catalysts: Nitrogen-Coordinated Ni Sites in Carbon-Based Materials for CO_2 Electroreduction. *Advanced Energy Materials* **2020**, *10*, 2001836.
15. Egerton, R. F.; Watanabe, M. Characterization of Single-Atom Catalysts by EELS and EDX Spectroscopy. *Ultramicroscopy* **2018**, *193*, 111–117.
16. Gao, Y.; Yang, Y.; Schimmenti, R.; Murray, E.; Peng, H.; Wang, Y.; Ge, C.; Jiang, W.; Wang, G.; DiSalvo, F. J.; Muller, D. A.; Mavrikakis, M.; Xiao, L.; Abruña, H. D.; Zhuang, L. A Completely Precious Metal–Free Alkaline Fuel Cell with Enhanced Performance Using a Carbon-Coated Nickel Anode. *Proceedings of the National Academy of Sciences* **2022**, *119*, e2119883119.
17. Li, Y.; Mohd Adli, N.; Shan, W.; Wang, M.; J. Zachman, M.; Hwang, S.; Tabassum, H.; Karakalos, S.; Feng, Z.; Wang, G.; C. Li, Y.; Wu, G. Atomically Dispersed Single Ni Site Catalysts for High-Efficiency CO_2 Electroreduction at Industrial-Level Current Densities. *Energy & Environmental Science* **2022**, *15*, 2108–2119.
18. Stöhr, J. *NEXAFS Spectroscopy*; Springer Series in Surface Science **25** (1992).
19. Lu, M.; Wang, J.; Fang, H.; Hu, Y.; Zhou, J. Unexpected Phase Separation in $Li_{1-x}Ni_{0.5}Mn_{1.5}O_4$ within a Porous Composite Electrode. *Chemical Communications* **2018**, *54*, 4152–4155.
20. Zheng, X.; Zhang, B.; De Luna, P.; Liang, Y.; Comin, R.; Voznyy, O.; Han, L.; García de Arquer, F. P.; Liu, M.; Dinh, C. T.; Regier, T.; Dynes, J. J.; He, S.; Xin, H. L.; Peng, H.; Prendergast, D.; Du, X.; Sargent, E. H. Theory-Driven Design of High-Valence Metal Sites for Water Oxidation Confirmed Using in Situ Soft X-Ray Absorption. *Nature Chem* **2018**, *10*, 149–154.
21. Lenser, C.; Lu, Q.; Crumlin, E.; Bluhm, H.; Yildiz, B. Charge Transfer Across Oxide Interfaces Probed by in Situ X-Ray Photoelectron and Absorption Spectroscopy Techniques. *J. Phys. Chem. C* **2018**, *122*, 4841–4848.
22. Huang, W.; Marcelli, A.; Xia, D. Application of Synchrotron Radiation Technologies to Electrode Materials for Li- and Na-Ion Batteries. *Advanced Energy Materials* **2017**, *7*, 1700460.
23. Zhong, J.; Deng, J.-J.; Mao, B.-H.; Xie, T.; Sun, X.-H.; Mou, Z.-G.; Hong, C.-H.; Yang, P.; Wang, S.-D. Probing Solid State N-Doping in Graphene by X-Ray Absorption near-Edge Structure Spectroscopy. *Carbon* **2012**, *50*, 335–338.
24. Liang, X.; Zhong, J.; Shi, Y.; Guo, J.; Huang, G.; Hong, C.; Zhao, Y. Hydrothermal Synthesis of Highly Nitrogen-Doped Few-Layer Graphene via Solid–Gas Reaction. *Materials Research Bulletin* **2015**, *61*, 252–258.
25. Regan, T. J.; Ohldag, H.; Stamm, C.; Nolting, F.; Lüning, J.; Stöhr, J.; White, R. L. Chemical Effects at Metal/Oxide Interfaces Studied by x-Ray-Absorption Spectroscopy. *Phys. Rev. B* **2001**, *64*, 214422.

26. Senkovskiy, B. V.; Usachov, D. Yu.; Fedorov, A. V.; Vilkov, O. Yu.; Shelyakov, A. V.; Adamchuk, V. K. Electronic Structure of Ti–Ni Alloys: An XPS and NEXAFS Study. *Journal of Alloys and Compounds* **2012**, *537*, 190–196.
27. Furlan, A.; Lu, J.; Hultman, L.; Jansson, U.; Magnuson, M. Crystallization Characteristics and Chemical Bonding Properties of Nickel Carbide Thin Film Nanocomposites. *J. Phys.: Condens. Matter* **2014**, *26*, 415501.
28. Krasnikov, S. A.; Sergeeva, N. N.; Brzhezinskaya, M. M.; Preobrajenski, A. B.; Sergeeva, Y. N.; Vinogradov, N. A.; Cafolla, A. A.; Senge, M. O.; Vinogradov, A. S. An X-Ray Absorption and Photoemission Study of the Electronic Structure of Ni Porphyrins and Ni N-Confused Porphyrin. *J. Phys.: Condens. Matter* **2008**, *20*, 235207.
29. Hitchcock, A. P.; Brion, C. E. Neon K-Shell Excitation Studied by Electron Energy-Loss Spectroscopy. *J. Phys. B: Atom. Mol. Phys.* **1980**, *13*, 3269–3273.
30. Sodhi, R. N. S.; Brion, C. E. Reference Energies for Inner Shell Electron Energy-Loss Spectroscopy. *Journal of Electron Spectroscopy and Related Phenomena* **1984**, *34*, 363–372.
31. Ma, Y.; Chen, C. T.; Meigs, G.; Randall, K.; Sette, F. High-Resolution K-Shell Photoabsorption Measurements of Simple Molecules. *Phys. Rev. A* **1991**, *44*, 1848–1858.
32. Hitchcock, A. P.; Ishii, I. Carbon K-Shell Excitation Spectra of Linear and Branched Alkanes. *Journal of Electron Spectroscopy and Related Phenomena* **1987**, *42* (1), 11–26.
33. Chen, C. T.; Ma, Y.; Sette, F. K-Shell Photoabsorption of the N2 Molecule. *Phys. Rev. A* **1989**, *40* (11), 6737–6740.
34. Hitchcock, A. P. aXis2000 is written in Interactive Data Language (IDL). It is available free for noncommercial use from http//unicorn.mcmaster. ca/aXis2000. html (accessed June 20, 2022)
35. Koprinarov, I. N.; Hitchcock, A. P.; McCrory, C. T.; Childs, R. F. Quantitative Mapping of Structured Polymeric Systems Using Singular Value Decomposition Analysis of Soft X-Ray Images. *J. Phys. Chem. B* **2002**, *106*, 5358–5364.
36. Hitchcock, A. P. Soft X-Ray Imaging and Spectromicroscopy. In *Handbook of Nanoscopy*; John Wiley & Sons, Ltd, **2012,** 745–791.
37. https://henke.lbl.gov/optical_constants/
38. https://www.britannica.com/science/nickel-chemical-element
39. Issa, S. A. M.; Darwish, A. A. A.; El-Nahass, M. M. The Evolution of Gamma-Rays Sensing Properties of Pure and Doped Phthalocyanine. *Progress in Nuclear Energy* **2017**, *100*, 276–282.
40. https://www.americanelements.com/nickel-sulfide-12035-72-2